Electric Power Systems Research 221 (2023) 109426

Contents lists available at ScienceDirect

Electric Power Systems Research

journal homepage: www.elsevier.com/locate/epsr

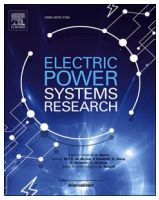

# A coordinated control hybrid MPPT algorithm for a grid-tied PV system considering a $V_{DC}I_Q$ control structure

Marta Haro-Larrode *, Ángel A. Bayod-Rújula

*Department of Electrical Engineering, Maria de Luna 3, 50018, School of Engineering and Architecture, University of Zaragoza, Zaragoza, Spain*

ARTICLE INFO

*Keywords:*
MPPT
Grid-connected PV system
Coordinated control
$V_{DC}I_Q$

ABSTRACT

In this paper, a new coordinated maximum power point tracking (MPPT) algorithm has been developed for a grid-tied PV system, whose inverter follows a $V_{DC}I_Q$ control scheme. The control objectives of this system are shared between 2 converters: a DC boost converter which performs MPPT of the PV plant, and an inverter which is responsible for DC voltage setpoint control, specific reactive current injection under request and reduced harmonic content of AC grid currents. The proposed algorithm operates upon a proper switching amongst conventional MPPT algorithms, namely perturb and observe (P&O) and incremental conductance (IC) algorithms, to take advantage of the best characteristics of each MPPT method with a different step size and considering the influence of the inverter control constants. Two coordination schemes are proposed for this algorithm to prioritise the improvement of different performance aspects over others. The impact of the proposed algorithm according to the 2 coordination schemes is evaluated and compared with the impact of conventional MPPT algorithms according to the trackability of power, the impact on DC voltage and on the AC grid side. The results are analysed by simulations conducted in MATLAB-Simulink.

## 1. Introduction

There are many types of maximum power point tracking (MPPT) algorithms that have been explored to improve the efficiency of PV power extraction. These can be classified according to different categories such as: bio-inspired [1–11], based on fuzzy logic (FL) [12–15], combinations of the previous ones [16–19] or conventional algorithms. The advantage of these bioinspired and FL-based MPPT methods is that they supposedly increase the efficiency and reliability of MPPT, but at the cost of increasing complexity, it turns out that they consume high computational resources when implementing them in real applications [20,21].

Amongst the conventional MPPT algorithms, the perturb and observe (P&O) and the incremental conductance (IC) algorithms are the most widely implemented algorithms in existing PV systems [22,23]. The basic version of P&O algorithm observes DC voltage coming from the PV solar panel and perturbs it until the maximum power point is reached for a given irradiance level [24]. Its main advantage is the simplicity of implementation, and the main disadvantage is the output power oscillation around maximum power point (MPP), thanks to which it is not suitable for rapidly changing irradiance levels [25]. The IC algorithm is based on the incremental comparison of the ratio of the derivative of conductance with the instantaneous conductance. The IC method overcomes the disadvantage of P&O method, as it reduces MPP oscillations during rapidly varying irradiance changes at a certain step size level [25]. These algorithms have been tested under dynamic environmental conditions and, while IC shows better efficiency than P&O, the performance of IC deteriorates more than of P&O for low irradiance levels, as concluded in [22]. Anyway, the operation of P&O and IC algorithms with fixed step size leads to a trade-off between speed of response and maximum steady-state power accuracy, as reported in [26]. This leads to the need of adaptive MPPT algorithms that combine these basic conventional algorithms with variable step size that enhance the tracking speed, reduce the oscillation around MPP and work well under deep irradiance level conditions.

In this sense, there have been several efforts in the literature to use conventional MPPT algorithms with a variable step size determined according to different techniques [6,7,26,27]. As for the IC method, in [6,7] adaptive scaling factors are proposed and estimated, on the one hand, via previous intensive simulations and according to different irradiance levels[6], and on the other hand, by employing an artificial neural network [7]. As for the P&O method, in [26,27], variable step sizes are calculated according on the one hand, to fuzzy logic and

* Corresponding author.
*E-mail addresses:* mharolarrode@unizar.es (M. Haro-Larrode), aabayod@unizar.es (Á.A. Bayod-Rújula).

https://doi.org/10.1016/j.epsr.2023.109426
Received 18 November 2022; Received in revised form 7 April 2023; Accepted 18 April 2023
Available online 29 April 2023

**Nomenclature**

| | |
|---|---|
| MPPT | Maximum power point tracking |
| $h_{IC}$ | Step size for (slow) $IC_1$ algorithm |
| $h_{P\&O}$ | Step size for (slow) $P\&O_1$ algorithm |
| $IC_1$ | (Slow) Incremental conductance method with $h_{IC}$ |
| $P\&O_1$ | (Slow) Perturb and Observe method with $h_{P\&O}$ |
| CS | Coordination scheme |
| $CS_1$ | Coordination scheme 1 |
| $CHA_1$ | Coordinated hybrid algorithm according to $CS_1$ |
| $G_1$ | Old value of irradiance ($W/m^2$) |
| δ | Magnitude of irradiance change |
| $T_{VDC}$ | Inverter outer loop control constant (ms) |
| $f_{s,inv}$ | Switching frequency of inverter (kHz) |
| $L_f$ | Output LCL filter inductance of inverter (μH) |
| $C_f$ | Output LCL filter capacitance of inverter (μF) |
| $R_f$ | Output LCL filter resistance of inverter (mΩ) |
| $k_{p,outer}$, $k_{i,outer}$ | Proportional and integral control parameters for outer loop of inverter |
| $k_{p,inner}$, $k_{i,inner}$ | Proportional and integral control parameters for inner loop of inverter |
| $k_{p,PLL}$, $k_{i,PLL}$ | Proportional and integral control parameters for PLL |
| $L_{boost}$ | DC boost converter inductance (mH) |
| $C_{boost}$ | DC boost converter capacitance (mF) |
| $f_{s,boost}$ | Switching frequency of DC boost converter (kHz) |
| $I_{PV}$ | Current signal from PV plant |
| $V_{PV}$ | Voltage signal from PV plant |
| $m_x$ | Modulation index for DC boost converter |
| $m_a$, $m_b$, $m_c$ | Modulation indices for inverter in abc frame |
| $m_d$, $m_q$ | Modulation indices for inverter in dq frame |
| $s_1 \ldots s_6$ | Gate signals to inverter's IGBTs |
| PCC | Point of common coupling |
| Vabc, Vdq | Voltage signals at PCC in abc and dq frames |
| PLL | Phase locked loop |
| MPP | Maximum power point |
| $5*h_{IC}$ | Step size for (fast) $IC_2$ algorithm |
| $50*h_{P\&O}$ | Step size for (fast) $P\&O_2$ algorithm |
| $IC_2$ | (Fast) Incremental conductance method with $5*h_{IC}$ |
| $P\&O_2$ | (Fast) Perturb and Observe method with $50*h_{P\&O}$ |
| $CS_2$ | Coordination scheme 2 |
| $CHA_2$ | Coordinated hybrid algorithm according to $CS_2$ |
| $G_2$ | New value of irradiance ($W/m^2$) |
| dG/dt | Irradiance change sign |
| $T_i$ | Inverter inner loop control constant (ms) |
| $N_p$ | Number of PV parallel strings |
| $N_s$ | Number of PV series modules per string |
| N | Total number of PV modules |
| $P_T$ | Total installed capacity of PV plant (kW) |
| $N_c$ | Number of cells per PV module |
| $V_{OC}$, $I_{SC}$ | Open-circuit voltage (V) and short circuit current (A) in a PV module under 1000 $W/m^2$ and 25 °C |
| $V_{MPP}$, $I_{MPP}$ | Maximum power point voltage (V) and current (A) under 1000 $W/m^2$ and 25 °C |
| $P_{MPP}$ | Maximum power value in a PV module under 1000 $W/m^2$ and 25 °C |
| $V_{AC\ grid}$ | AC grid phase to phase voltage (V) |
| $f_{AC\ grid}$ | AC grid frequency (Hz) |
| SCR | AC grid short-circuit ratio |
| $V_{DC}$ | DC voltage signal measured at the output of the DC boost converter |
| $V_{DC,ref}$ | DC voltage reference |
| $I_{d,ref}$, $I_{q,ref}$ | d-and q-axis current reference |
| $I_d$, $I_q$ | Measured d- and q-current signals at the output of the inverter and before LCL filter |
| $V_d$, $V_q$ | Measured d- and q-voltage signals at PCC |
| $\theta_{grid}$ | AC grid phase |
| Iabc, Idq | Current signals before LCL filter in abc and dq frames |

non-switching zone schemes [26], and on the other hand, according to a backstepping algorithm [27].

In [28], a coordinated control strategy based on pure P&O control and DC voltage regulation algorithm was proposed for a grid-tied PV system, but no further innovations were made on the MPPT algorithm. The authors in [29] designed a hybrid MPPT algorithm based on conventional ones, built upon P&O combined with open circuit voltage and short-circuit current that led to the enhancement of the tracking capability and efficiency MPPT process, but neither the impact on DC voltage nor the influence of an AC grid was studied.

However, the design of an MPPT algorithm for an AC grid-tied PV installation should also enhance the compliance with AC grid code requirements, as stated in [30]. In this sense, different MPPT algorithms could impact better than others on the power quality of AC current waveforms, as it was previously explored in [31] with a hybrid MPPT algorithm based on artificial neural networks (ANN) and P&O techniques. However, the impact of an MPPT algorithm on the AC grid side or DC voltage side has not been sufficiently studied in the literature and very few authors monitor the impact of the MPPT algorithm on the DC voltage [32], on the power quality injected AC current waveforms [31] or even on the AC grid frequency behaviour [33]. Therefore, in this paper an MPPT algorithm for the DC-DC converter is evaluated jointly with the control time constants of the inverter to optimize not only the behaviour of the extracted DC power and voltage from the PV plant, but also the power quality level of the injected AC currents to the AC grid.

The paper is organized as follows: in Section 2 the proposed coordinated algorithm (CHA) is described, as well as the proposed coordination schemes. In Section 3, the grid-tied PV based system under study is described. In Section 4, the impact of the proposed CHA is evaluated according to the trackability of DC power, influence on DC voltage and impact on the AC grid side. A discussion is achieved amongst the proposed CHA and the conventional MPPT algorithms. In Section 5, a sensitivity analysis is performed on the time constants of $V_{DC}I_Q$ scheme. In Section 6, the results are compared with other works in the literature and in Section 7 the main conclusions are extracted.

## 2. The new coordinated control hybrid MPPT algorithm (CHA)

In this section the proposed CHA for MPPT is described. Its working principle is based on the proper coordination of pure P&O and IC algorithms with different step sizes to benefit from the strengths of each one.

A previous comparative analysis was carried out to understand the strengths and weaknesses between P&O and IC algorithms with different step sizes. However, and since the comparison will be indeed achieved in Section 4, this previous analysis has not been included. The timing that rules the switching between one algorithm and the following one is determined by the variation regime of the irradiance and by the outer loop time constant of the inverter, $T_{VDC}$. Both factors affect the calculation of timing points after one algorithm gets deactivated and before the next one is activated.

From now on, the basic step sizes for slower P&O and IC algorithms, i.e. $P\&O_1$ and $IC_1$, are defined as $h_{P\&O} = 10^{-4}$ and $h_{IC}$=0.1. Larger step sizes, i.e. $50*h_{P\&O}$ and $5*h_{IC}$, correspond to faster P&O and IC algorithms, i.e. $P\&O_2$ and $IC_2$. To explore different potentialities of the proposed CHA, two coordination schemes (CSs) are proposed to enhance

different performance criteria with respect to pure P&O and IC algorithms.

On the one hand, the coordinated hybrid algorithm according to $CS_1$ ($CHA_1$) prioritises the time to reach the full DC power setpoint value during sharp rises of irradiance and this value is achieved with less overshoot than $P\&O_2$ algorithms. Besides, it minimises the error of DC output power to the setpoint at steady state conditions and keeps it at the lowest value during profound irradiance changes. During deep drops in irradiance, the algorithm prioritises the crossing time to the full power setpoint with less overshoot than IC algorithms.

On the other hand, the coordinated hybrid algorithm according to coordination scheme 2 ($CHA_2$) prioritises the time to reach the 95% value of the DC power setpoint during sharp irradiance rises and this is achieved with less overshoot than $CHA_1$ and $P\&O_2$. In turn, it provides greater error level at the high-level irradiance steady-state value. During deep drops, it guarantees lower overshoot than $CHA_1$ but slower convergence time.

The flowcharts of $CHA_1$ and $CHA_2$ are shown in Fig. 1, where the sequences of algorithms according to different magnitudes and signs of irradiance change are included.

In this sense, $CHA_1$ and $CHA_2$ act as upper control entities whose coordination structure implies the sequence of different basic P&O and IC algorithms, whenever the irradiance suffers from changes. The sequence of algorithms whenever there is an irradiance change is achieved within a time window determined by the value of the time constant of grid-side inverter outer loop, $T_{VDC}$. Specifically, the time window is calculated as the sum of $T_{VDC}$ plus the rise or fall time of irradiance, estimated by photodiode sensors. The scheme in Fig. 1 is explained as follows. As shown in Fig. 1, the parameter δ is used to distinguish between profound and superficial changes, which represents the irradiance threshold jump between one instant and the next. If the irradiance jump exceeds threshold δ, the change is considered to be profound, giving rise to either a sharp rise or a deep drop, depending on the sign of the derivative of G. On the other hand, if the jump in irradiance does not exceed the threshold δ, the changes are considered to be superficial. In principle, δ was given a value of 200 $W/m^2$, being this as sufficient change to make the difference between the two categories.

Therefore, $CHA_1$ and $CHA_2$ start receiving the irradiance measurement signal, G, and whenever an irradiance change ($|G_1\text{-}G_2|$) is sufficiently small ($|G_1\text{-}G_2| < \delta$), $IC_2$ algorithm is gets activated within both $CHA_1$ and $CHA_2$. However, when a sufficiently large change in irradiance is detected ($|G_1\text{-}G_2| > \delta$), the sign of dG/dt is calculated and from now on, $CHA_1$ and $CHA_2$ follow different sequences of P&O and IC algorithms.

If dG/dt has a negative sign, a deep drop of irradiance is occurring, and within $CHA_1$ the sequence of algorithms starts with $IC_1$, and this operates during the fall time to the setpoint plus the time delay due to the inverter $T_{VDC}$ time constant. Afterwards, $CHA_1$ switches to $P\&O_2$. In contrast, $CHA_2$ starts with $P\&O_2$. This algorithm is active during the fall time to the setpoint plus $T_{VDC}$. Afterwards, $IC_2$ comes into operation.

In case of dG/dt=0, there would be no variation of algorithm, and the operating algorithm in that case would be the last selected one.

The output of each selected algorithm is connected to the power electronic stage, namely to the converter that transforms duty cycle inputs to gate signals to control the transistor of DC-DC converter. These outputs have not been represented in the diagrams, in view of the visual complexity that would involve. However, the basic algorithms ($P\&O_1$, $P\&O_2$, $IC_1$ and $IC_2$) do not exchange information or data with each other. The arrows connecting them mean just a sequential order decided upon the coordination scheme, according to the irradiance jumps and irradiance signs.

## 3. Application case

The grid-tied PV system is divided into a PV side and grid side converters, as represented in Fig. 2, and has been implemented in MATLAB-Simulink. The PV side includes the PV installation and a DC boost converter that carries out maximum power point tracking (MPPT) to the PV plant. Thus, the DC boost converter conveys the maximum energy extracted from the PV plant to the grid-side converter. The PV plant is implemented as an aggregated model composed by a set of individual PV modules and strings. The DC boost converter is controlled by means of the MPPT controller. The MPPT controller includes the proposed CHA, where the basic P&O and IC algorithms have been implemented via duty cycle modification in MATLAB embedded functions.

The AC grid side includes an inverter that receives the energy transferred by the DC boost converter and injects it into the AC grid after an LCL filter action. The inverter is controlled according to a $V_{DC}I_Q$ cascaded control structure based on PI regulators. Such structure is composed by an outer loop, responsible for the tracking of the DC

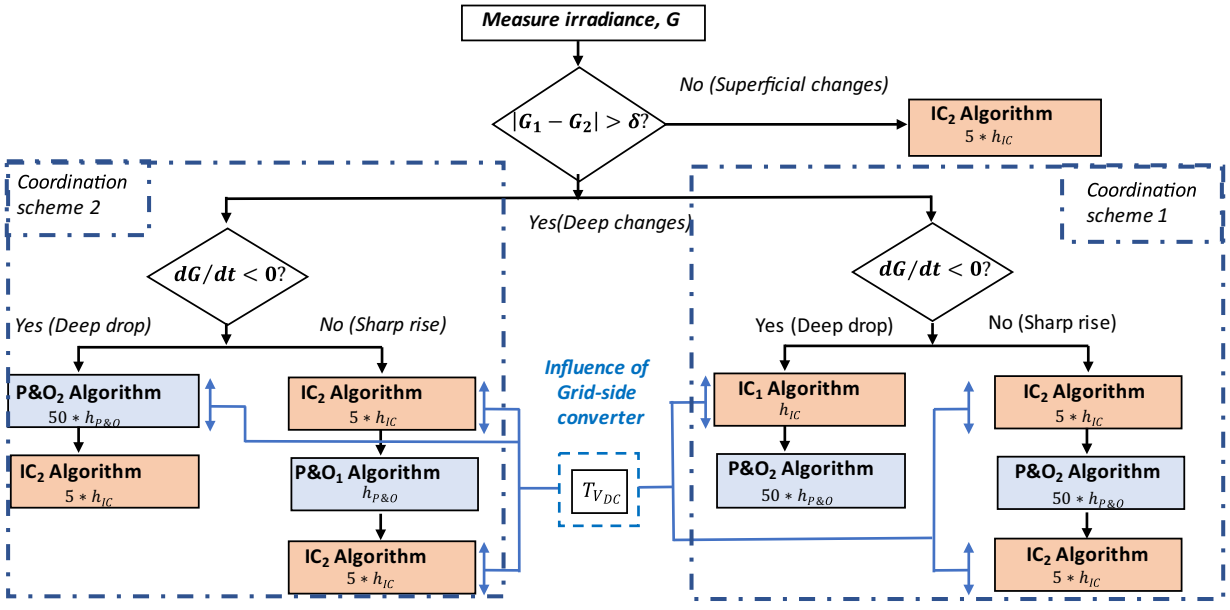


**Fig. 1.** New hybrid MPPT according to two coordination schemes ($CHA_1$ and $CHA_2$).

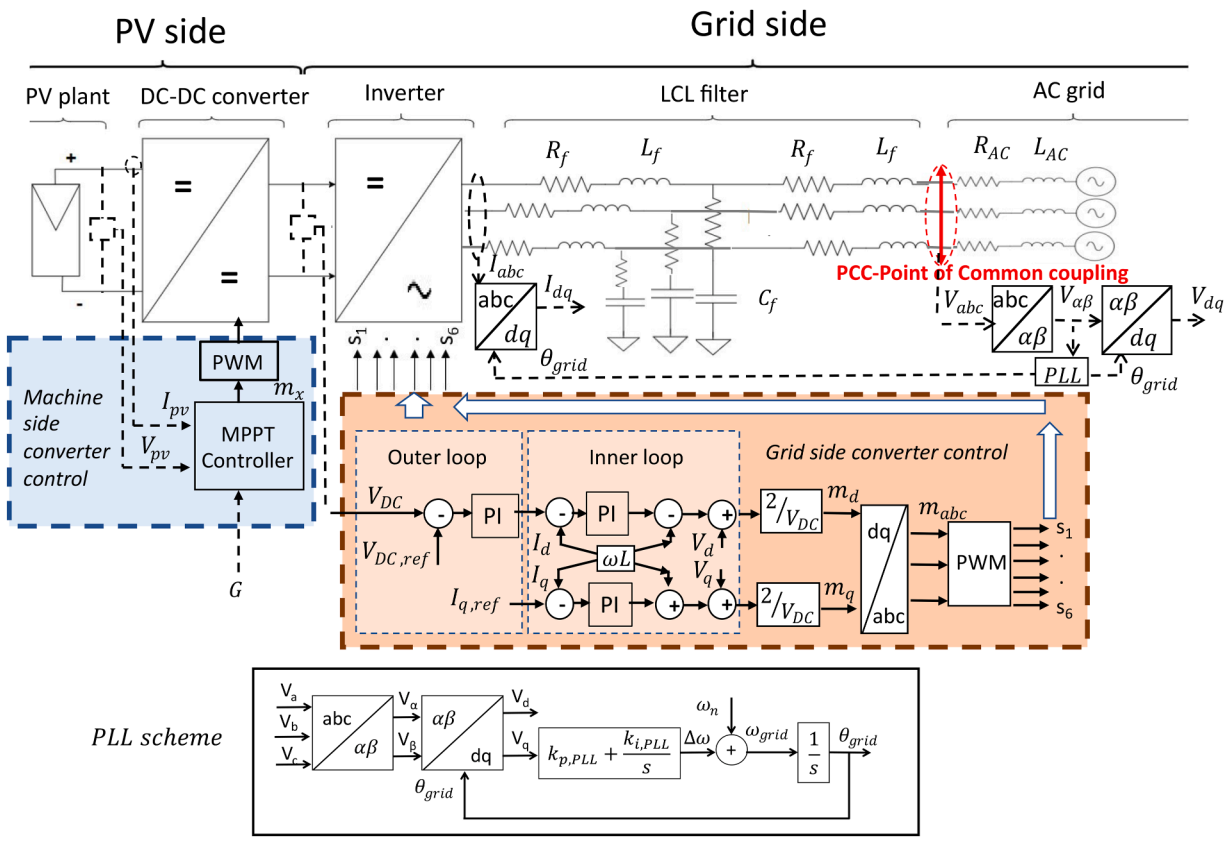


**Fig. 2.** Grid-tied PV system under study.

voltage setpoint, and two inner loops, in charge of controlling the d and q current signals. The AC grid is modelled by means of a wye-connected voltage sources characterized by $R_{AC}$ and $L_{AC}$. As shown in Fig. 2, the necessary transformations from abc to dq coordinates are made by Park and Clarke transforms. The grid phase angle, $\theta_{grid}$, is captured by means of a PLL) scheme that follows a synchronous reference frame (SRF) structure [34]. This PLL scheme is selected due to the effective decoupling of d and q components of grid voltage.

The complete set of parameters that define the system in Fig. 2 are included in Table 1. The units of these parameters are indicated in the nomenclature section.

## 4. Simulation and impact of the proposed CHA

In this section, $CHA_1$ and $CHA_2$ are evaluated according to the trackability of the MPP, impact on DC voltage control and on the AC grid side. Such evaluation is achieved comparatively with conventional P&O and IC algorithms.

### 4.1. Trackability of the MPP

The trackability of the DC output power measured at the output of the DC boost converter is evaluated under a variable irradiance pattern that lasts 1 s. In Fig. 3, the DC output power signal is showed for the $CHA_1$ and $CHA_2$ -driven systems, as well as for the PV systems driven by conventional algorithms.

As for sharp rises, it is necessary to carefully analyse the time stretches between $t = 0$ s and $t = 0.25$ s, and from $t = 0.85$ and $t = 1$ s in Fig. 3. Within these time stretches, $P\&O_2$ crosses the setpoint with certain overshoot, but it is the fastest algorithm in reaching the full setpoint value as well. Besides, $P\&O_1$ algorithm is the one that reaches the 95% of setpoint value most rapidly but the convergence to steady state value is slower than with $P\&O_2$.

Furthermore, $P\&O_1$ presents the greatest steady state error. On the other hand, IC algorithms present an intermediate speed of response between the $P\&O_1$ and $P\&O_1$. However, $IC_2$ presents the lowest error with respect to the setpoint, and $IC_1$ presents undesired wide amplitude steady state oscillations.

Therefore, $CHA_1$ takes advantage of the fast arrival to full setpoint given by $P\&O_2$ algorithm but with lower overshoot than $P\&O_2$ and from the minimised error to setpoint given by $IC_2$ algorithm. However, $CHA_1$ is slow at reaching the 95% of setpoint value.

In turn, $CHA_2$ takes advantage of the fastest arrival to 95% of the setpoint value given by $P\&O_1$ but it presents greater steady-state error to setpoint than $IC_2$ and $CHA_1$ algorithms. As for deep drops, it is necessary to carefully analyse the time stretch between $t = 0.65$ s and $t = 0.85$ s in

**Table 1**
Parameters of the complete system presented in Fig. 2.

| PV module characteristics | | PV plant parameters | | Inverter parameters | | | | PLL and AC grid parameters | | DC-DC boost converter | |
|---|---|---|---|---|---|---|---|---|---|---|---|
| $N_c$ | 60 | $N_p$ | 47 | $f_{s,inv}$ (kHz) | 10 | $k_{p,outer}$ | 2 | $k_{p,PLL}$ | 10 | $f_{s,boost}$ (kHz) | 5 |
| $V_{OC}$ (V) | 36.3 | $N_s$ | 10 | $L_f$ (μH) | 250 | $k_{i,outer}$ | 100 | $k_{i,PLL}$ | 50,000 | $L_{boost}$ (mH) | 4 |
| $I_{SC}$ (A) | 7.84 | N | 470 | $C_f$ (μF) | 100 | $k_{p,inner}$ | 10 | $f_{AC\ grid}$ (Hz) | 50 | $C_{boost}$ (mF) | 12 |
| $V_{MPP}$ (V) | 29 | $P_T$ (kW) | 100.18 | $R_f$ (mΩ) | 1 | $k_{i,inner}$ | 2000 | $V_{AC\ grid}$ (V) | 400 | | |
| $I_{MPP}$ (A) | 7.35 | | | | | | | SCR | 10 | | |
| $P_{MPP}$ (W) | 213.15 | | | | | | | | | | |

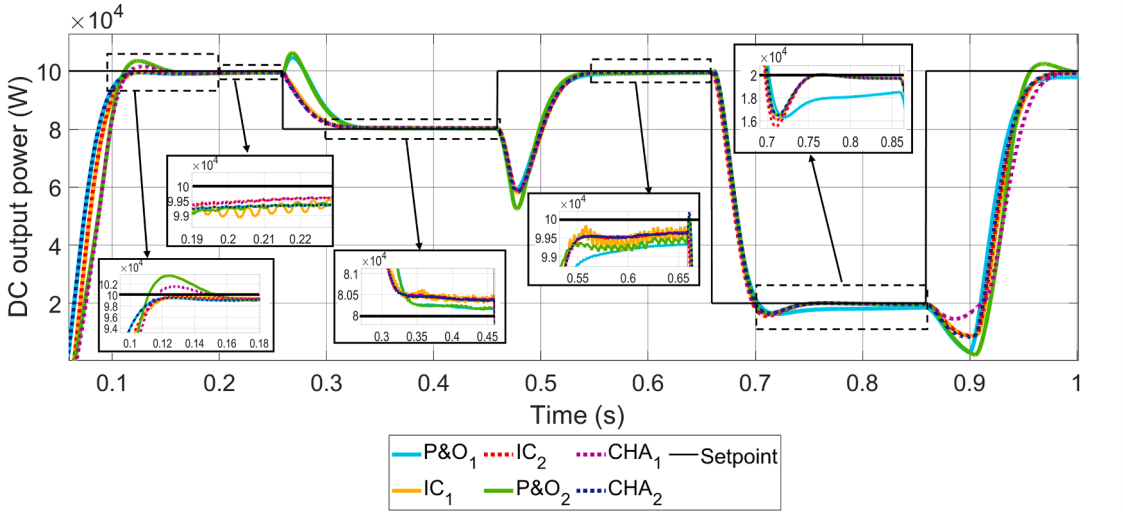


**Fig. 3.** Output DC power signals of DC boost converter with different MPPT algorithms.

Fig. 3. $P\&O_1$ reaches the setpoint with the slowest speed, but it also yields to the lowest overshoot amplitude level.

However, it also presents the largest error to setpoint during low level steady-state conditions. In contrast, $IC_2$ algorithm is the fastest in reaching the setpoint, but it presents the largest overshoot amplitude. In the middle of these two behaviours lie $P\&O_2$ and $IC_1$ algorithms. Both present lower oscillation than $IC_2$ and converge rapidly to steady-state value. Therefore, $CHA_1$ takes advantage of the lower overshoot amplitude of $IC_1$ and of the rapid convergence to steady state with low steady-state error of $P\&O_2$. In contrast, $CHA_2$ takes advantage of the even lower overshoot amplitude of $P\&O_2$ compared to IC algorithms and the low error of $IC_2$ during steady-state conditions.

As for superficial changes, it is necessary to carefully analyse the time stretches between $t = 0.25$ s and $t = 0.65$ s in Fig. 3. P&O algorithms present greater overshoot during setpoint changes than IC algorithms. Apart from this, $IC_1$ algorithm, despite its fast convergence time to setpoint, presents a high content of wide-amplitude oscillations during steady-state regime. This has also been observed within sharp rises. Therefore, $IC_2$ is the one that best performs during these superficial and rapid changes in irradiance. $CHA_1$ and $CHA_2$ take advantage of several features provided by $IC_2$, such as the fast convergence time to steady state value, the low steady-state error, and the low content of steady-state oscillations.

### 4.2. Impact on DC voltage

In Fig. 4, the DC voltage signals of the PV systems driven by the different MPPT algorithms, namely, $IC_1$, $P\&O_1$, $IC_2$, $P\&O_2$, $CHA_1$ and $CHA_2$ are compared. It can be visibly noted that $IC_1$ presents the highest content of steady-state DC voltage ripple, in comparison to the other algorithms. This jointly with the high content of steady-state oscillations in DC power makes $IC_1$ algorithm inadequate for steady-state conditions at high irradiance levels and only feasible for transient conditions of deep drops and low irradiance levels where no steady state oscillations appear.

In contrast, $P\&O_1$ presents the lowest content in DC voltage ripple during the whole simulation. $P\&O_2$ presents the highest overshoot during irradiance changes and the second largest DC voltage ripple magnitude. In turn, $IC_2$, $CHA_1$ and $CHA_2$ present a lower DC voltage ripple than $P\&O_2$ and $IC_1$, but higher than $P\&O_1$. Overall, CHA algorithms present a low level of ripple amplitude but higher than the value provided by $P\&O_1$ algorithm.

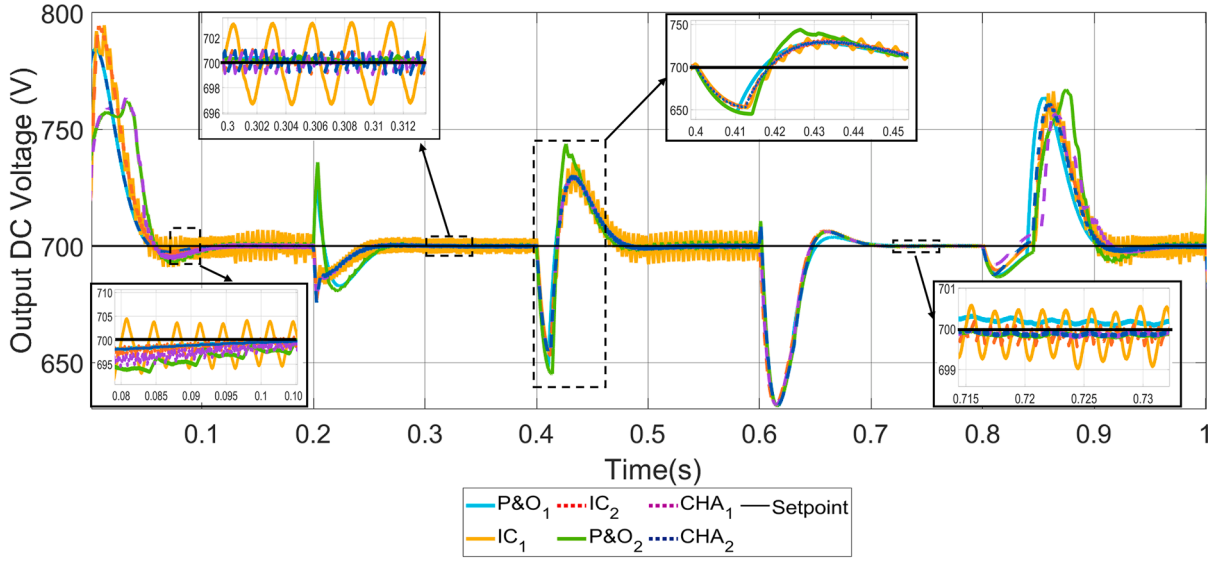


**Fig. 4.** Output DC voltage signals with different MPPT algorithms.

### 4.3. Impact on the AC grid side

Overall, the impact of the proposed $CHA_1$ and $CHA_2$ on the transient behaviour of AC grid voltages and currents is very similar. For this reason, the current and voltage signals of only the $CH_1$-driven system at different points on the AC grid is shown in Fig. 5.

In Fig. 5(a) and (b) the current signals in abc stationary frame before LCL filter and at PCC, respectively. In the zoomed area of Fig. 5(a), distorted waveforms are shown, while in the zoomed area of Fig. 5 (b), the distortion of waveforms is much lower than in Fig. 5(a). In Fig. 5(c), the voltage signals in abc coordinates at PCC are shown and the voltage waveforms present negligible distortion.

However, the harmonic content of current signals differs from one algorithm to another. In Fig. 6, total harmonic distortion (THD) is calculated for current waveforms at the output of the inverter (before LCL filter) and at PCC.

According to Fig. 6(a) and (b), there are two main peaks located around the instants 0.65 and 0.85 s of simulation, which correspond to a deep droop and sharp rise, respectively.

Both $CHA_1$ and $CHA_2$ exceed the 5% of THD of current signals before

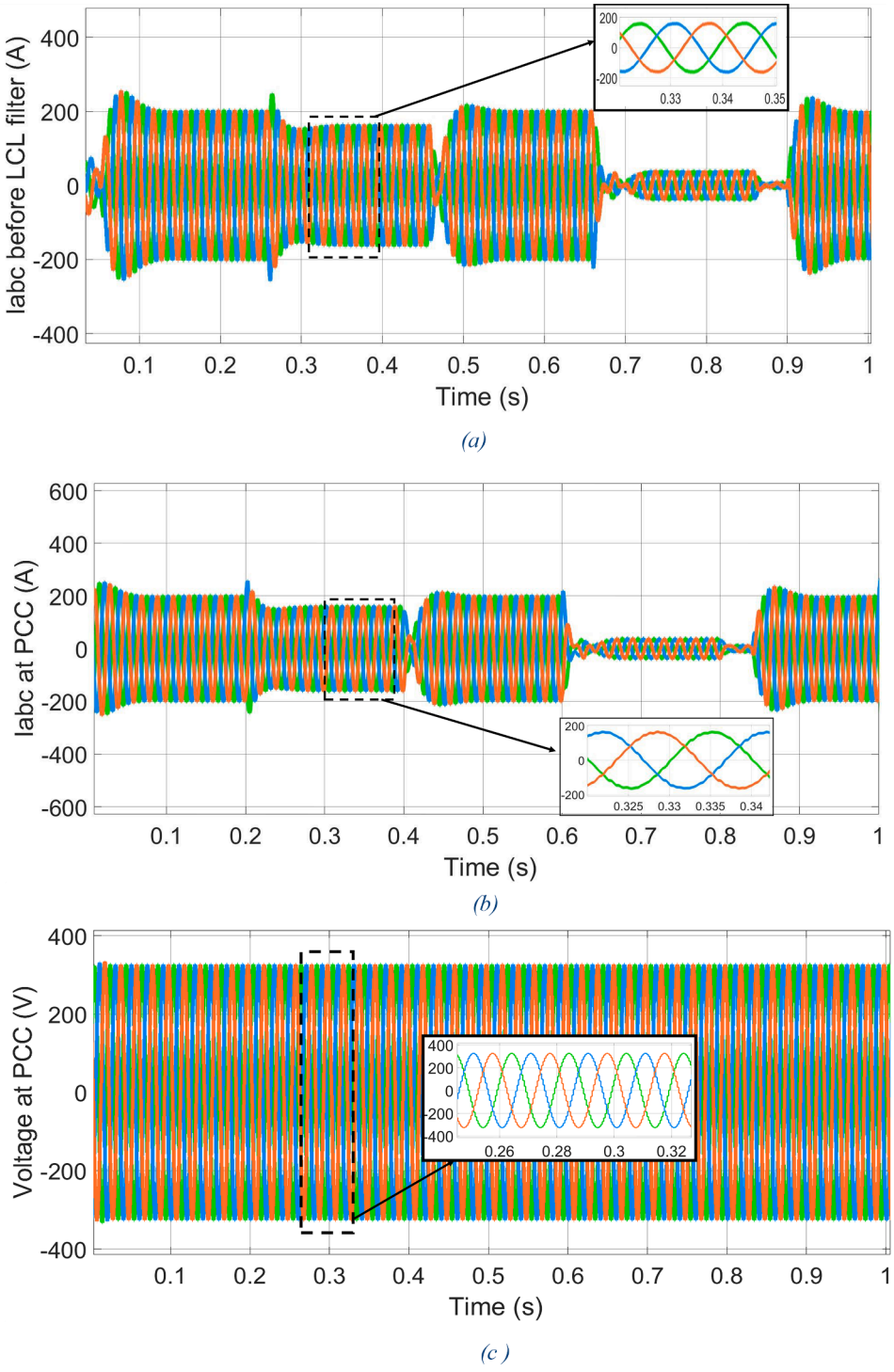


**Fig. 5.** Current and voltage signals in abc stationary frame at the AC side: (a) Current signals at the output of the inverter and before LCL filter, (b) Current signals at the PCC and (c) Voltage signals at the PCC.

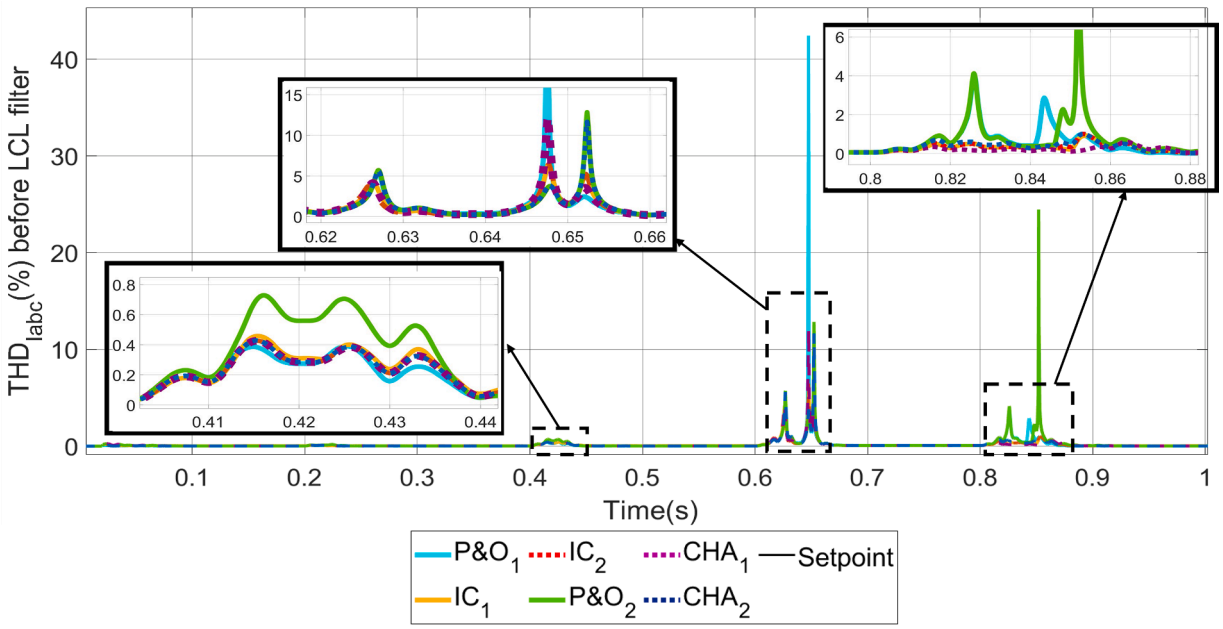


*(a)*

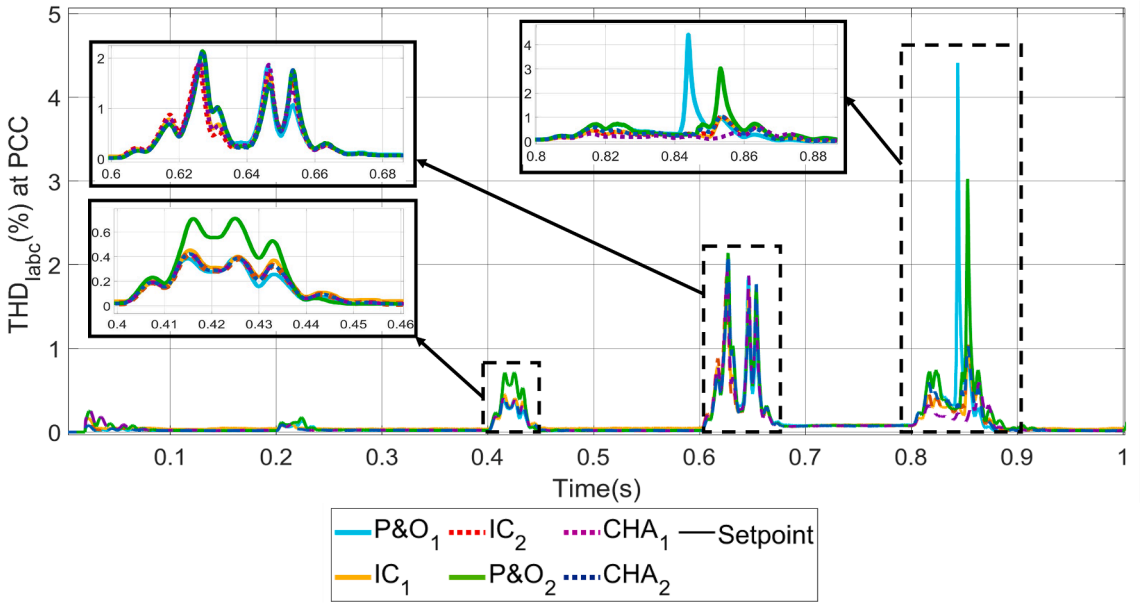


*(b)*

**Fig. 6.** Total harmonic distortion (THD)signal of current waveforms measured at: (a) the output of inverter and before LCL filter and (b) at PCC.

LCL filter around the instant at $t = 0.65$ s by reaching values around 10%. During deep irradiance changes, P&O algorithms exceed the 5% threshold by much margin than $CHA_1$ and $CHA_2$, by obtaining more than 40% of current THD in the worst case. Nevertheless, at around $t = 0.85$ s both $CHA_1$ and $CHA_2$ keep the current THD before LCL filter much below the 5% threshold. On the contrary, $P\&O_2$ algorithm widely exceeds the 5% threshold at the sharp rise by reaching almost the 25% of THD value. In Fig. 6(b), every THD current value after LCL filter present values below the 5% threshold. However, P&O algorithms get closer to the threshold in the surroundings of the sharp rise, whereas $CHA_1$ and $CHA_2$ and IC algorithms present much lower values of THD during the sharp rise.

The different duty cycle manipulation achieved by P&O and IC algorithms and step sizes are responsible for the different THD level on the PCC current waveforms. Besides, since $CHA_1$ and $CHA_2$ include dynamics originated from coordination schemes, one may think that $CHA_1$ and $CHA_2$ algorithms could imply worse harmonic distortion on current waveforms during sharp rises and deep drops of irradiance. However, and as seen in Fig. 6, $CHA_1$ and $CHA_2$ do not have worse impact on harmonics than basic P&O and IC algorithms. Around $t = 0.85$ s, the algorithms that imply worst THD impact are $P\&O_1$ and $P\&O_2$. In contrast, hybrid $CHA_1$ and $CHA_2$ and basic $IC_1$ and $IC_2$ lead to lower harmonic distortion. Therefore, the hybridization of P&O with IC algorithms is beneficial, since the THD level of current waveforms is reduced due to the influence of IC algorithms.

### 4.4. Discussion

The algorithms are now compared under sharp rises, deep drops and superficial changes by using numerical data enclosed in Table 2 and

**Table 2**
Numerical values for each performance criterion during sharp rises and deep drops of irradiance.

| Performance criteria | Sharp rises | | | | | | Deep drops | | | | | |
|---|---|---|---|---|---|---|---|---|---|---|---|---|
| | $P\&O_1$ | $IC_1$ | $IC_2$ | $P\&O_2$ | $CHA_1$ | $CHA_2$ | $P\&O_1$ | $IC_1$ | $IC_2$ | $P\&O_2$ | $CHA_1$ | $CHA_2$ |
| Time to cross 95% of DC power setpoint (s) | 0.0427 | 0.0469 | 0.046 | 0.0472 | 0.0472 | 0.0427 | 0.0383 | 0.0357 | 0.0347 | 0.0371 | 0.0357 | 0.0371 |
| Time to cross 100% of DC power setpoint (s) | – | – | – | 0.1114 | 0.1164 | – | 0.04363 | 0.0398 | 0.0384 | 0.0413 | 0.0398 | 0.0413 |
| DC power negative/positive overshoot amplitude(kW) | 17 | 11.2 | 11.2 | 18/3.5 | 7/1 | 11.6/0 | 3.7 | 3.9 | 4.5 | 3.555 | 3.75 | 3.5 |
| Maximum DC power point (kW) at $t = 0{,}19$ s, 0.79s | 99.39 | 99.7 | 99.61 | 99.417 | 99.645 | 99.39 | 18.5 | 19.74 | 19.74 | 19.74 | 19.74 | 19.74 |
| DC power steady-state error (%) | 0.61 | 0.3 | 0.39 | 0.583 | 0.3 | 0.61 | 7.5 | 1.3 | 1.3 | 1.3 | 1.3 | 1.3 |
| DC power oscillation amplitude(W) | 70 | 400 | 70 | 200 | 70 | 70 | 30 | 30 | 30 | 30 | 30 | 30 |
| DC power Oscillation period (ms) | 2.5 | 4.7 | 2.5 | 6.5 | 2.5 | 2.5 | <0.1 | <0.1 | <0.1 | <0.1 | <0.1 | <0.1 |
| DC voltage ripple amplitude(V) | 0.16 | 12.2 | 2.2 | 2.5 | 2.2 | 0.16 | 0.025 | 1.3 | 0.4 | 0.025 | 0.025 | 0.025 |
| DC voltage ripple period (ms) | <0.1 | 4.25 | 0.7 | 6.7 | 0.7 | <0.1 | <0.1 | 2 | <0.1 | <0.1 | <0.1 | <0.1 |
| THD in current waveforms before LCL filter (%) | 2.9 | 0.95 | 1 | 24.45 | 0.59 | 1 | 42.43 | 6.45 | 6.45 | 12.83 | 12 | 11.65 |

**Table 3**
Numerical values for each performance criterion during superficial changes of irradiance.

| Performance criteria | Superficial changes | | | | | | | | | | | |
|---|---|---|---|---|---|---|---|---|---|---|---|---|
| | $P\&O_1$ | | $IC_1$ | | $IC_2$ | | $P\&O_2$ | | $CHA_1$ | | $CHA_2$ | |
| Time to cross 95% of DC power setpoint (s) | 0.124 | | 0.114 | | 0.11 | | 0.124 | | 0.11 | | 0.11 | |
| Time to cross 100% of DC power setpoint (s) | – | | – | | – | | – | | – | | – | |
| DC power negative/positive overshoot amplitude (kW) | 21 | | 21.6 | | 21.6 | | 27.5 | | 21.6 | | 21.6 | |
| Maximum power point (kW) at $t = 0.39$ s and $t = 0.59$s | 80.2 | 99.3 | 80.4 | 99.6 | 80.4 | 99.4 | 80.2 | 99.4 | 80.4 | 99.6 | 80.4 | 99.6 |
| DC power steady-state error (%) | −0.25 | 0.7 | −0.5 | 0.4 | −0.5 | 0.4 | −0.25 | 0.6 | −0.5 | 0.4 | −0.5 | 0.4 |
| DC power Oscillation amplitude (W) | 80 | | 150 | | 80 | | 80 | | 80 | | 80 | |
| DC power Oscillation period (ms) | 3.2 | | 2.4 | | 3.2 | | 3.2 | | 3.2 | | 3.2 | |
| DC voltage ripple amplitude (V) | 0.09 | | 6.9 | | 1.6 | | 1.6 | | 1.6 | | 1.6 | |
| DC voltage ripple period (ms) | <0.1ms | | 2.72 | | 0.7 | | 6 | | 0.7 | | 0.7 | |
| THD in current waveforms before LCL filter (%) | 0.38 | | 0.45 | | 0.42 | | 0.72 | | 0.42 | | 0.42 | |

Table 3. These data are also presented in polygons in Fig. 7, where the central positions (0–2) indicate better performance than those positions on the peripheral marks (5–6). As seen in Tables 2 and 3, and Figs. 7 and 8, $CHA_1$ and $CHA_2$ improve the performance over basic algorithms according to:

- THD in current waveforms before LCL filter (%). Within the sharp rise, $CHA_1$ and $CHA_2$ reach 0.59% and 1%, respectively, against the maximum of 24.45% reached by $P\&O_2$. Within deep drops, $CHA_1$ and $CHA_2$ reach 12 and 11.65% for of THD, respectively, against 42.43% reached by $P\&O_1$. Within deep drops IC algorithms reach the lowest harmonic content with 6.45% of THD. Within superficial changes, while $CHA_1$ and $CHA_2$ present a lower value of 0.42%, $P\&O_2$ algorithm reaches the highest THD value of 0.72%.
- DC voltage ripple amplitude and period. During the sharp rise, the DC voltage ripple amplitude is improved from 12.2 V, achieved by $IC_1$, to 0.16 V, achieved by $CHA_2$. Within deep drops, $CHA_1$ and $CHA_2$ reach an amplitude of 0.025 V against 1.3 V reached by $IC_1$ algorithm, and present a period lower than 0.1 ms, against 2 ms reached by $IC_1$ algorithm. Within superficial changes, though $CHA_1$ and $CHA_2$ present a low DC voltage ripple amplitude value of 1.6 V, $P\&O_1$ algorithm present an even lower value of 0.09 V. As for the period, within the sharp rise and the deep drop, $CHA_1$ and $CHA_2$ get the lowest ripple period compared to the rest of algorithms. Within superficial irradiance changes, $CHA_1$ and $CHA_2$ present a period of 0.7 ms compared to 6 ms reached by $P\&O_2$ algorithm.
- DC power oscillation amplitude and period. Within the sharp rise, while IC algorithms present up to 400 W of power oscillation amplitude, $CHA_1$ and $CHA_2$ only present 70 W. Besides, these oscillations present period of up to 2.5 ms against 6.5 ms reached by $P\&O_2$. For a deep drop, the six MPPT algorithms behave similarly, reaching 30 W of amplitude value and an oscillation period lower than 0.1 ms
- DC power positive or negative overshoot amplitude. Within a sharp rise, $CHA_1$ and $CHA_2$ reach a positive amplitude up of 1 kW and 0 kW, respectively, compared to 3.5 kW reached by $P\&O_2$; and a negative amplitude of 7 kW and 11.6 kW respectively, compared to 18 kW reached by $P\&O_2$. Within deep drops, $CHA_1$ and $CHA_2$ reach an amplitude up to 3.75 and 3.5 kW respectively, against 4.5 kW reached by $IC_2$. Within superficial changes, $CHA_1$ and $CHA_2$ present an overshoot amplitude in DC power of 21.6 kW, compared to $P\&O_2$, that presents 27.5 kW.
- DC power steady-state error. Within the deep drop, $CHA_1$ and $CHA_2$ reach 1.3% value, against 7.5% reached by $P\&O_1$.

There is just a pair of criteria within superficial irradiance changes, where a basic MPPT algorithm, $P\&O_1$, achieves better performance than $CHA_1$ and $CHA_2$. $P\&O_1$ reaches the lowest DC voltage ripple period and THD level within superficial irradiance changes, but with no significant difference with respect $CHA_1$ and $CHA_2$. Aside of this exception, $CHA_1$ and $CHA_2$ behave better in the remaining criteria.

Besides, $CHA_1$ and $CHA_2$ are distinguished from each other in the following criteria:

- Time to cross 95% of DC power setpoint value. Within the sharp rise, while $CHA_2$ reaches the lowest time value, 0.0427 s, $CHA_1$ and $P\&O_2$ reach the highest value, 0.0472 s. Within the deep drop, while $CHA_1$ reaches a lower time value, 0.0357 s, $CHA_2$ reaches a higher value, 0.0371 s. However, $IC_2$ is the fastest algorithm with a time mark of 0.0347 s. Within superficial changes, $CHA_1$ and $CHA_2$ reach the 95% value in 0.11 s, compared to $P\&O_2$, that reaches it in 0.124 s
- Time to cross 100% of DC power setpoint value. Within the sharp rise, $CHA_1$ and $P\&O_2$ cross the 100% value of setpoint by 0.1114 and 0.1164s, respectively, whereas the rest of algorithms do not reach this value. Within a deep drop, a similar rank is obtained.
- DC power steady state error. Within the sharp rise, $CHA_1$ reaches the lowest error, around 0.3%, jointly with IC algorithms. In turn, $CHA_1$ and P&O algorithms reach the highest error values, up to 0.61%. For a superficial drop, $CHA_1$ and $CHA_2$ present a steady-state error of −0.5% against −0.25% presented by P&O algorithms. This is seen as

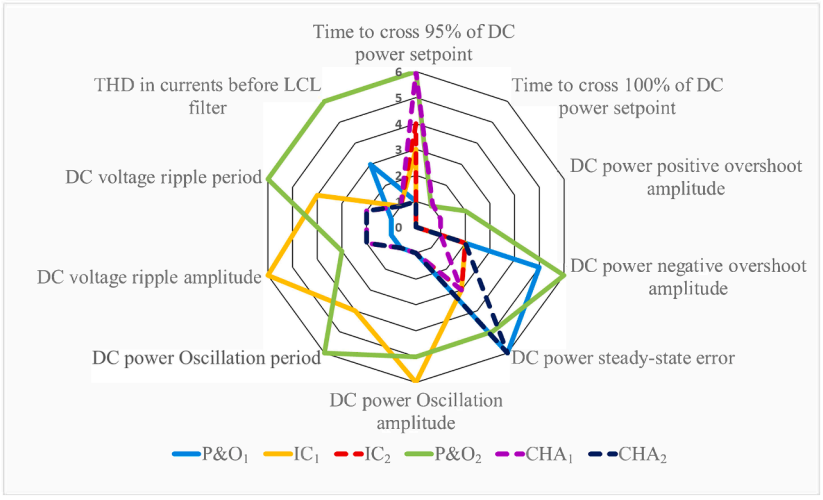


(a)

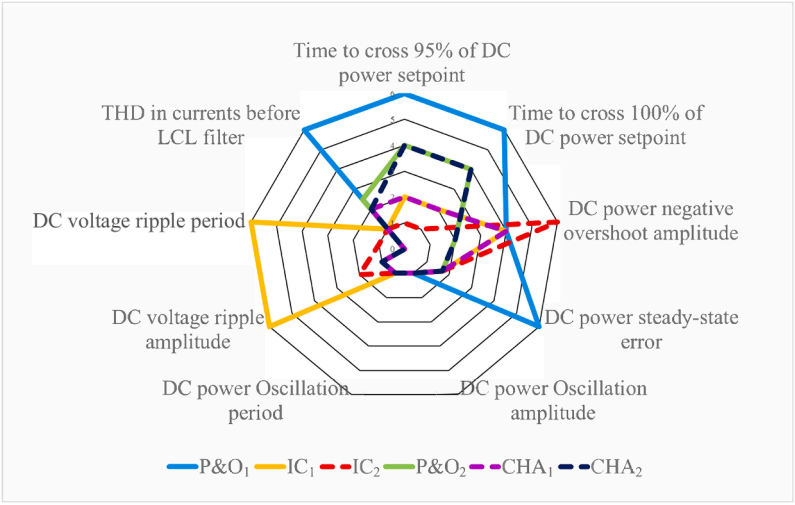


(b)

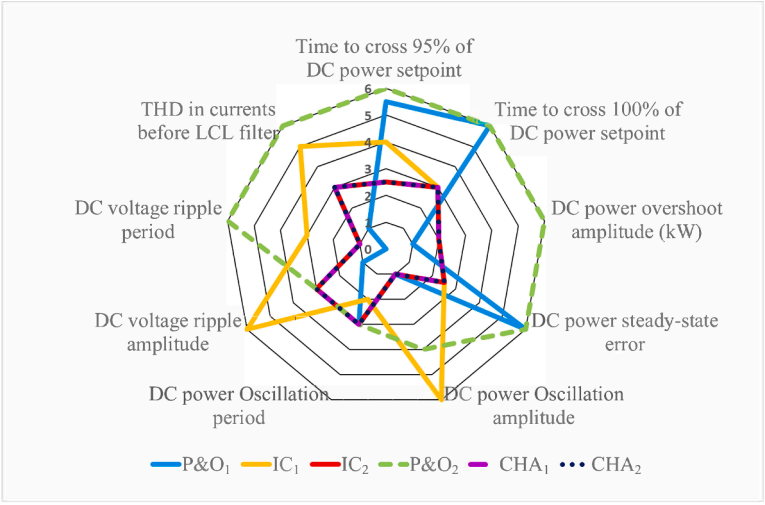


(c)

**Fig. 7.** Comparative polygons for $CHA_1$, $CHA_2$, P&O and IC algorithms during: (a) sharp rises, (b) deep drops and (c)superficial changes of irradiance.

an advantage as it maximizes output power. For a superficial rise, $CHA_1$ and $CHA_2$ present an error of 0.4% against 0.7% reached by $P\&O_1$.

## 5. Sensitivity analysis for the proposed CHA MPPT algorithm

The response of the $CHA_1$ -driven system under a different $V_{DC}I_Q$ control structure is tested in Fig. 8(a) and (b), where the influence of $T_{VDC}$ on the DC power and voltage is revealed, respectively. The

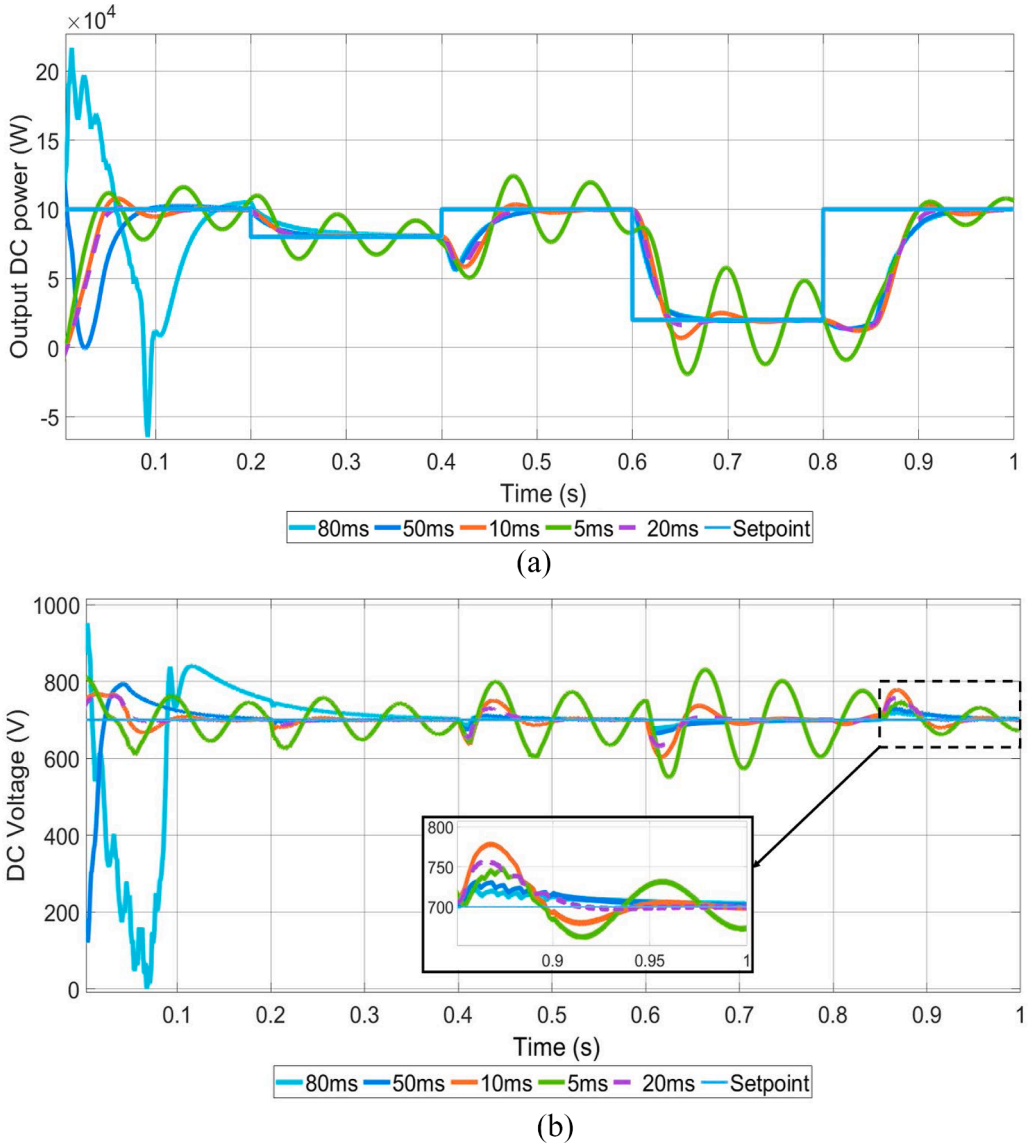


**Fig. 8.** Influence of outer loop time constant on the: (a)output DC power and (b) output DC voltage of the DC boost converter for the system driven by $CHA_1$ algorithm.

behaviour of $CHA_2$-driven system has not been shown, due to the similarity with the dynamics in Fig. 8. Those $T_{VDC}$ values greater than the inner loop time constant, $T_i$ =5 ms, but lower than 80 ms guarantee an adequate DC power and voltage responses. The case of $T_{VDC}$ =5 ms provides the fastest dynamics, but with large oscillations, which compromises stability.The best cases for outer loop $T_{VDC}$ constants are the design value, 20 ms. and 10 ms, as they yield to lower overshoot in DC voltage and power, and they turn to be greater than Ti. However, large $T_{VDC}$ constants such as 50 ms or 80 ms yield to a slow response with very poor tracking capabilities.

## 6. Comparison with other works in the literature

In [18], a comparative analysis of MPPT algorithms was achieved, considering P&O, FL and ANN techniques, under others. The authors in [18] implemented a similar irradiance pattern but their PV plant present much lower power capacity, 14 PV modules and 3430 W for maximum power point, compared with 470 modules and 100.18 kW of maximum power point in this paper. Time responses up to 29.16 ms are claimed in [18], lower in comparison with the values obtained in the present paper, namely up to 42.7 ms during a sharp rise, and up to 35.7 ms during a deep drop, achieved by $CHA_2$ and $CHA_1$ algorithms, respectively.

It is important to note that in [18], only a DC side connection is included, and no AC-side converter control influence is considered. Besides, the switching frequency of the DC converter in [18] is 50 kHz, which much greater in comparison with 5 kHz used for the DC converter in the present paper. Considering that the inverse of the switching frequency represents a time delay, this is an influencing factor that affects the final time response of each MPPT algorithm. In the present paper, two commutation frequency values of PV-side and grid-side converters, 5 kHz and 10 kHz, respectively, have been considered. These lead to commutation delays of 200 and 100 μs, respectively. According to [29], a digital time delay of a basic processor would imply just low microseconds, which can be considered very low compared to the commutation delay of PV-side converter considered in this paper, 200 μs. A similar conclusion is obtained when comparing the present paper with [15].

As for the accuracy of algorithms, the authors in [18] claim errors up to 3.81%, while in this paper $CHA_1$ and $CHA_2$ reach 1.3% in deep drops, 0.3 and 0.61% respectively in a sharp rise. The range of errors given in [18] for a P&O algorithm span from 0.95% to 1.34% and for FL algorithm, from 0.59% to 3.84%. Therefore, the range of steady-state error

of the proposed CHAs improves the range obtained in [18]. In contrast, in [31], a more similar installation is considered with 432 PV modules and both DC-DC converters and AC-grid side inverter. The authors in [31] claim an efficiency of 98.26%, which corresponds to an error of 1.74%. In the present paper, the errors oscillate within a range, depending on the variation regime of irradiance. In [31], measurements have been achieved based on superficial changes of irradiance, being irradiance changes 200 W/m$^2$ wide. In our paper, the errors during superficial irradiance jumps range from 0.4 to 0.5%, during sharp rise, between 0.3% and 0.61%, and during a deep droop around 1.3%.

Different harmonic peaks exceeding the 5% threshold were also pinpointed in the current waveforms before LCL filter during deep irradiance changes in [31]. In the present paper, during similar deep irradiance changes, THD values around the 10% are obtained for $CHA_1$ and $CHA_2$, but P&O algorithms always get worse results. Anyway, the current waveforms after the LCL filtering stage in the present paper present levels lower than 5% regardless of the considered irradiance regime.

As for the implementation cost, $CHA_1$ and $CHA_2$ do not involve more complex operations than those involved by the cited methods in other papers, such as in [29]. As for the number of sensors, the proposed algorithms would imply having photodiodes to measure irradiance summed to the usual voltage and current sensors required in these installations. Anyway, these implementation needs would be compensated with the advantages provided by the proposed algorithms over the basic ones. Such investment would be justified due to the capacity of the PV plant, which is 100 kW.

## 7. Conclusions

In this paper a coordinated control MPPT algorithm has been proposed to extract the maximum power of a grid-tied PV installation by means of the proper switching between basic MPPT algorithms. The prioritisation of different features that shape the DC power behaviour has yielded to 2 coordination schemes, $CHA_1$ and $CHA_2$, upon which the hybrid algorithm is constructed. The results indicate that $CHA_1$ and $CHA_2$ improve the overall efficiency of the system and improve rising and falling time responses either to the 95% or full DC power setpoint values. Besides, the DC voltage and power ripple amplitude, period and the THD level in output current waveforms are overall decreased by CHA structure compared to P&O algorithms during deep irradiance changes. The hybridization of P&O with IC algorithms has been shown to be beneficial, since the THD level of current waveforms is reduced due to the influence of IC algorithms. Besides, the influence of inverter control constants has been assessed.

## CRediT authorship contribution statement

**Marta Haro-Larrode:** Conceptualization, Methodology, Software, Validation, Formal analysis, Writing – original draft. **Ángel A. Bayod-Rújula:** Writing – review & editing, Visualization.

## Declaration of Competing Interest

The authors declare that they have no known competing financial interests or personal relationships that could have appeared to influence the work reported in this paper.

## Data availability

Data will be made available on request.

## References


[1] H. Elaissaoui, M. Zerouali, A. el Ougli, B. Tidhaf, MPPT Algorithm Based on Fuzzy Logic and Artificial Neural Network (ANN) for a Hybrid Solar/Wind Power Generation System, in: 4th International Conference on Intelligent Computing in Data Sciences, ICDS 2020, Oct. 2020, https://doi.org/10.1109/ICDS50568.2020.9268747.

[2] S. Negri, F. Giani, N. Blasuttigh, A.M. P.avan, A. Mellit, E. Tironi, Combined model predictive control and ANN-based forecasters for jointly acting renewable self-consumers: an environmental and economical evaluation, Renew. Energy (Jul. 2022), https://doi.org/10.1016/j.renene.2022.07.065.

[3] M. Dhimish, V. Holmes, B. Mehrdadi, M. Dales, Comparing Mamdani Sugeno fuzzy logic and RBF ANN network for PV fault detection, Renew. Energy 117 (Mar. 2018) 257–274, https://doi.org/10.1016/j.renene.2017.10.066.

[4] L.L. J.iang, D.R. N.ayanasiri, D.L. M.askell, D.M. V.ilathgamuwa, A hybrid maximum power point tracking for partially shaded photovoltaic systems in the tropics, Renew. Energy 76 (Apr. 2015) 53–65, https://doi.org/10.1016/j.renene.2014.11.005.

[5] W.K. Y.ap, V. Karri, An off-grid hybrid PV/diesel model as a planning and design tool, incorporating dynamic and ANN modelling techniques, Renew. Energy 78 (Jun. 2015) 42–50, https://doi.org/10.1016/j.renene.2014.12.065.

[6] M.T. C.huang, Y.H. L.iu, S.P. Y.e, A Novel Variable Step Size Incremental Conductance Method with an Adaptive Scaling Factor, Appl. Sci. 10 (15) (Jul. 2020) 5214, https://doi.org/10.3390/APP10155214. *2020, Vol. 10, Page 5214*.

[7] P. Liu, et al., Artificial Neural Network Assisted Variable Step Size Incremental Conductance MPPT Method with Adaptive Scaling Factor, Electronics (Basel) 11 (1) (Dec. 2021) 43, https://doi.org/10.3390/ELECTRONICS11010043. *2022, Vol. 11, Page 43*.

[8] M. Mao, L. Zhang, Q. Duan, B. Chong, Multilevel DC-link converter photovoltaic system with modified PSO based on maximum power point tracking, Solar Energy 153 (Sep. 2017) 329–342, https://doi.org/10.1016/j.solener.2017.05.017.

[9] N. Sa-ngawong, I. Ngamroo, Intelligent photovoltaic farms for robust frequency stabilization in multi-area interconnected power system based on PSO-based optimal Sugeno fuzzy logic control, Renew. Energy 74 (Feb. 2015) 555–567, https://doi.org/10.1016/j.renene.2014.08.057.

[10] K. Sundareswaran, V. Vignesh kumar, S. Palani, Application of a combined particle swarm optimization and perturb and observe method for MPPT in PV systems under partial shading conditions, Renew. Energy 75 (Mar. 2015) 308–317, https://doi.org/10.1016/J.RENENE.2014.09.044.

[11] J. Shi, W. Zhang, Y. Zhang, F. Xue, T. Yang, MPPT for PV systems based on a dormant PSO algorithm, Electr. Power Syst. Res. 123 (Jun. 2015) 100–107, https://doi.org/10.1016/J.EPSR.2015.02.001.

[12] X. Li, H. Wen, Y. Hu, L. Jiang, A novel beta parameter based fuzzy-logic controller for photovoltaic MPPT application, Renew. Energy 130 (Jan. 2019) 416–427, https://doi.org/10.1016/j.renene.2018.06.071.

[13] G.I. G.iurgi, L.A. S.zolga, D.V. G.iurgi, Benefits of Fuzzy Logic on MPPT and PI Controllers in the Chain of Photovoltaic Control Systems, Appl. Sci. 12 (5) (Feb. 2022) 2318, https://doi.org/10.3390/APP12052318. *2022, Vol. 12, Page 2318*.

[14] A. Saleh, K.S. F.aiqotul Azmi, T. Hardianto, W. Hadi, Comparison of MPPT fuzzy logic controller based on perturb and observe (P&O) and incremental conductance (InC) algorithm on buck-boost converter, in: Proceedings - 2018 2nd International Conference on Electrical Engineering and Informatics: Toward the Most Efficient Way of Making and Dealing with Future Electrical Power System and Big Data Analysis, ICon EEI 2018, Oct. 2018, pp. 154–158, https://doi.org/10.1109/ICON-EEI.2018.8784324.

[15] U. Yilmaz, O. Turksoy, A. Teke, Improved MPPT method to increase accuracy and speed in photovoltaic systems under variable atmospheric conditions, Int. J. Electr. Power Energy Syst. 113 (Dec. 2019) 634–651, https://doi.org/10.1016/j.ijepes.2019.05.074.

[16] A. Belaout, F. Krim, A. Mellit, B. Talbi, A. Arabi, Multiclass adaptive neuro-fuzzy classifier and feature selection techniques for photovoltaic array fault detection and classification, Renew. Energy 127 (Nov. 2018) 548–558, https://doi.org/10.1016/j.renene.2018.05.008.

[17] M. Lasheen, M. Abdel-Salam, Maximum power point tracking using Hill Climbing and ANFIS techniques for PV applications: a review and a novel hybrid approach, Energy Convers. Manag. 171 (Sep. 2018) 1002–1019, https://doi.org/10.1016/j.enconman.2018.06.003.

[18] M.I.S. Guerra, F.M.U. de Araújo, M. Dhimish, R.G. V.ieira, Assessing Maximum Power Point Tracking Intelligent Techniques on a PV System with a Buck–Boost Converter, Energies 14 (22) (Nov. 2021) 7453, https://doi.org/10.3390/EN14227453. *2021, Vol. 14, Page 7453*.

[19] S.D. A.l-Majidi, M.F. A.bbod, H.S. A.l-Raweshidy, Design of an Efficient Maximum Power Point Tracker Based on ANFIS Using an Experimental Photovoltaic System Data, Electronics (Basel) 8 (8) (Aug. 2019) 858, https://doi.org/10.3390/electronics8080858.

[20] S. Sarwar, M.A. H.afeez, M.Y. J.aved, A.B. A.sghar, K. Ejsmont, A Horse Herd Optimization Algorithm (HOA)-Based MPPT Technique under Partial and Complex Partial Shading Conditions, Energies (Basel) 15 (5) (Mar. 2022) 1880, https://doi.org/10.3390/en15051880.

[21] M.A. M.ohamed, A.A. Z.aki Diab, H. Rezk, Partial shading mitigation of PV systems via different meta-heuristic techniques, Renew. Energy 130 (Jan. 2019) 1159–1175, https://doi.org/10.1016/j.renene.2018.08.077.

[22] K. Ishaque, Z. Salam, G. Lauss, The performance of perturb and observe and incremental conductance maximum power point tracking method under dynamic weather conditions, Appl. Energy 119 (Apr. 2014) 228–236, https://doi.org/10.1016/J.APENERGY.2013.12.054.

[23] M. Abdel-Salam, M.T. E.l-Mohandes, M. Goda, An improved perturb-and-observe based MPPT method for PV systems under varying irradiation levels, Solar Energy 171 (Sep. 2018) 547–561, https://doi.org/10.1016/J.SOLENER.2018.06.080.
[24] M. Kamran, M. Mudassar, M.R. F.azal, M.U. A.sghar, M. Bilal, R. Asghar, Implementation of improved Perturb & Observe MPPT technique with confined search space for standalone photovoltaic system, J. King Saud Univ. - Eng. Sci. 32 (7) (Nov. 2020) 432–441, https://doi.org/10.1016/J.JKSUES.2018.04.006.
[25] Á.A. B.ayod-Rújula, J.A. C.ebollero-Abián, A novel MPPT method for PV systems with irradiance measurement, Solar Energy 109 (1) (Nov. 2014) 95–104, https://doi.org/10.1016/J.SOLENER.2014.08.017.
[26] N.S. D.'Souza, L.A.C. Lopes, X.J. L.iu, Comparative study of variable size perturbation and observation maximum power point trackers for PV systems, Electr. Power Syst. Res. 80 (3) (Mar. 2010) 296–305, https://doi.org/10.1016/J.EPSR.2009.09.012.
[27] A. Charaabi, A. Zaidi, O. Barambones, N. Zanzouri, Implementation of adjustable variable step based backstepping control for the PV power plant, Int. J. Electr. Power Energy Syst. 136 (Mar. 2022), 107682, https://doi.org/10.1016/J.IJEPES.2021.107682.
[28] M. Lakshmi, S. Hemamalini, Coordinated control of MPPT and voltage regulation using single-stage high gain DC–DC converter in a grid-connected PV system, Electr. Power Syst. Res. 169 (Apr. 2019) 65–73, https://doi.org/10.1016/J.EPSR.2018.12.011.
[29] A.F. M.urtaza, M. Chiaberge, F. Spertino, U.T. S.hami, D. Boero, M. De Giuseppe, MPPT technique based on improved evaluation of photovoltaic parameters for uniformly irradiated photovoltaic array, Electr. Power Syst. Res. 145 (Apr. 2017) 248–263, https://doi.org/10.1016/J.EPSR.2016.12.030.
[30] S.B. S.kretas, D.P. P.apadopoulos, Efficient design and simulation of an expandable hybrid (wind–photovoltaic) power system with MPPT and inverter input voltage regulation features in compliance with electric grid requirements, Electr. Power Syst. Res. 79 (9) (Sep. 2009) 1271–1285, https://doi.org/10.1016/J.EPSR.2009.03.010.
[31] Ö. Çelik, A. Teke, A Hybrid MPPT method for grid connected photovoltaic systems under rapidly changing atmospheric conditions, Electr. Power Syst. Res. 152 (Nov. 2017) 194–210, https://doi.org/10.1016/j.epsr.2017.07.011.
[32] D. Nguyen, G. Fujita, Analysis of sensorless MPPT method for hybrid PV–Wind system using DFIG Wind Turbines, Sustain. Energy, Grids Netw. 5 (Mar. 2016) 50–57, https://doi.org/10.1016/J.SEGAN.2015.11.001.
[33] B.A. B.astiani, R.V. d.e Oliveira, Adaptive MPPT control applied to virtual synchronous generator to extend the inertial response of type-4 wind turbine generators, Sustain. Energy, Grids Netw. 27 (Sep. 2021), 100504, https://doi.org/10.1016/J.SEGAN.2021.100504.
[34] R. Panigrahi, S.K. M.ishra, S.C. S.rivastava, A.K. S.rivastava, N.N. S.chulz, Grid Integration of Small-Scale Photovoltaic Systems in Secondary Distribution Network - A Review, IEEE Trans. Ind. Appl. 56 (3) (May 2020) 3178–3195, https://doi.org/10.1109/TIA.2020.297978.